RSC Advances

ROYAL SOCIETY OF CHEMISTRY

PAPER

View Article Online
View Journal | View Issue

Check for updates

Cite this: *RSC Adv.*, 2022, **12**, 29151

# Achieving stable photoluminescence by double thiacalix[4]arene-capping: the lanthanide-oxo cluster core matters†

Zixiu Lu,[ab] Shujian Wang,[ab] Zhu Zhuo,[cd] Guo-Ling Li,[cd] Haomiao Zhu,[cd] Wei Wang,*[cd] You-Gui Huang*[cde] and Maochun Hong[abd]

Received 7th August 2022
Accepted 3rd October 2022

DOI: 10.1039/d2ra04942b

rsc.li/rsc-advances

Luminescence stability is a critical consideration for applying phosphors in practical devices. In this work, we report two categories of double *p-tert*-butylthiacalix[4]arene ($H_4TC4A$) capped clusters that exhibit characteristic lanthanide luminescence. Specifically, $\{[Ln_4(\mu_4\text{-}OH)(TC4A)_2(DMF)_6(CH_3OH)_3(HCOO)Cl_2]\}\cdot xCH_3OH$ (Ln = Eu (**1**), Tb (**2**); $x$ = 0–1) with square-planar $[Ln_4(\mu_4\text{-}OH)]$ cluster cores and $\{[Ln_9(\mu_5\text{-}OH)_2(\mu_3\text{-}OH)_8(OCH_3)(TC4A)_2(H_2O)_{24}Cl_9]\}\cdot xDMF$ (Ln = Gd (**3**), Tb (**4**), Dy (**5**); $x$ = 2–6) with hourglass-like $[Ln_9(\mu_5\text{-}OH)_2(\mu_3\text{-}OH)_8]$ cluster cores are synthesized and characterized. By comparing **2** and **4**, we find that several critical luminescence properties (such as quantum efficiency and luminescence stabilities) depend directly on the cluster core structure. With the square-planar $[Ln_4(\mu_4\text{-}OH)]$ cluster cores, **2** demonstrates high quantum yield (∼65%) and excellent luminescence stability against moisture, high temperature, and UV-radiation. A white light-emitting diode (LED) with ultrahigh color quality is successfully fabricated by mixing **2** with commercial phosphors. These results imply that high quality phosphors might be achieved by exploiting the double thiacalix[4]arene-capping strategy, with an emphasis on the cluster core structure.

## Introduction

Polynuclear lanthanide clusters possess interesting structures, leading to unique physical and chemical properties, such as magnetism, luminescence, catalysis, and so on.[1–10] Among these different properties, photoluminescence of the lanthanide-oxo clusters is of particular interest and has been widely investigated.[11–15] In homometallic lanthanide clusters, the 4f orbitals of $Ln^{3+}$ ions are shielded by the $5s^25p^6$ subshells and therefore give highly intensive narrow-band emissions, making them attractive for a wide range of applications such as displays, luminescent sensors, and medical-probes for clinical use.[9,10,14] Famous examples include $Eu^{3+}$ and $Tb^{3+}$ based clusters with red ($^5D_0 \rightarrow {}^7F_n$ transition) and green ($^5D_4 \rightarrow {}^7F_n$ transition) luminescence, respectively.[9,13] One common problem related to the photoluminescence of traditional lanthanide clusters is their decreasing emission intensity in moisture, high temperature, or continuous UV exposure.[16–19] The development of stable and efficient lanthanide-cluster phosphors for practical application is still an ongoing challenge.

To improve the luminescence stability, different extrinsic modification strategies, such as compositing, surface engineering, and device encapsulation, *etc.*, have been developed to in the past few years.[20–25] For example, Chen and coworkers[26] prepared uniform $CsPbX_3$/polyacrylonitrile nanofibers by an electrospinning technique and the hydrophobic polyacrylonitrile provides superior resistance towards humidity; Liu *et al.*[27] blended pre-synthesized $CsPbBr_3$ PQDs with porous silica spheres (pore size: 12–15 nm) to obtain composites showing enhanced thermal stability and photo-stability. However, parasitic problems are often observed because of these extrinsic strategies. For examples, (1) the physical properties of the material (*e.g.* electroconductivity), may decrease significantly after applying polymer or inorganics coating; (2) the surface treatment for achieving a complete coating could be cumbersome; (3) although these methods maybe effective in improving moisture stability, the luminescent stability under high temperature might remain poor if only the external coatings were applied.[28] Therefore, instead of applying preventative

---

[a] *School of Rare Earth, University of Science and Technology of China, Ganzhou, China*
[b] *Ganjiang Innovation Academy, Chinese Academy of Sciences, Ganzhou 341000, China*
[c] *CAS Key Laboratory of Design and Assembly of Functional Nanostructures, Fujian Provincial Key Laboratory of Nanomaterials, Fujian Institute of Research on the Structure of Matter, Chinese Academy of Sciences, China. E-mail: wangwei@fjirsm.ac.cn; yghuang@fjirsm.ac.cn*
[d] *Xiamen Key Laboratory of Rare Earth Photoelectric Functional Materials, Xiamen Institute of Rare Earth Materials, Haixi Institutes, Chinese Academy of Sciences, Xiamen, Fujian 361021, China*
[e] *Fujian Science & Technology Innovation Laboratory for Optoelectronic Information of China, Fuzhou, 350108, China*

† Electronic supplementary information (ESI) available: The crystallographic data; the selected bond distances table; the selected bond valence analysis; the decay analysis data; XRD; SEM; IR; excitation spectra; the decay curves; TG-DSC. CCDC 2189240–2189244. For ESI and crystallographic data in CIF or other electronic format see DOI: **https://doi.org/10.1039/d2ra04942b**

measures extrinsically, it might be more effective to develop rational synthetic routes for clusters with tailored structures and compositions, which could intrinsically enhance the luminescence stability of lanthanide-oxo clusters.

One of the effective method to stabilize polynuclear clusters is by introducing supporting ligands. *p-tert*-Butylthiacalix[4]arene ($H_4TC4A$), a macrocyclic tetramers of phenols joined by sulfur atoms, has been recognized as a good choice for capturing polynuclear clusters and cages by its multiple phenolic hydroxyl groups.[29,30] An important feature of this ligand is that it participates in the coordination *via* one side, leaving the other side exposed with a large number of hydrophobic tertiary-butyl-groups. Because of the multiple coordination sites, a series of polynuclear nanoclusters or nanocages, including $\{Mn_{16}\}$,[31] $\{Co_{32}\}$,[32] $\{Ni_{18}\}$,[33] $\{Ni_{32}\}$,[34] $\{Ni_{40}\}$,[35] and $\{Ag_{88}\}$,[36] have been reported. Comparing with transition metal ions, $H_4TC4A$-protected homometallic lanthanide nanoclusters are still rudimentary. Only $H_4TC4A$-capped $\{Ln_4\}$ (Ln = Tb, Dy)[37] and $\{Ln_5\}$ (Ln = Dy, Ho, Er)[38] nanoclusters have been reported. Moreover, the luminescent properties and stabilities of these $H_4TC4A$-capped clusters have not been extensively discussed, not to mention the relationship between the polynuclear cluster core structures and their luminescent characteristics. So, it is crucial to investigate $H_4TC4A$-capped lanthanide nanoclusters with different lanthanide-oxo cluster cores, to establish a systematic understand of the structural impact of the polynuclear cores to the photoluminescence properties and stabilities.[39]

In this work, we obtain two types of distinct double-$H_4TC4A$-capped clusters, $\{Ln_4\}$ (Ln = Tb **1**, Eu **2**) and $\{Ln_9\}$ (Ln = Dy **3**, Tb **4**, Gd **5**) *via* solvothermal synthesis. Both of the square-planar $[Ln_4(\mu_4\text{-}OH)]$ cluster cores (structure **1–2**) and the hourglass-like $[Ln_9(\mu_5\text{-}OH)_2(\mu_3\text{-}OH)_8]$ cluster cores (structure **3–5**) are capped by two $H_4TC4A$ ligands to form double-capped structures. The luminescent properties and stabilities of these lanthanide clusters is investigated, with an emphasis on exploring the structure–property relationships of their luminescence and stabilities.

# Experimental

## Chemicals

Commercial chemicals, $EuCl_3\cdot 6H_2O$ (Adamas Co., Ltd., >99.0%), $GdCl_3\cdot 6H_2O$ (Adamas Co., Ltd., 99.9%), $TbCl_3\cdot 6H_2O$ (Adamas Co., Ltd., 99.9%), $DyCl_3\cdot 6H_2O$ (Adamas Co., Ltd., 99.99%), $Ni(NO_3)_2\cdot 6H_2O$ (Adamas Co., Ltd., 99.99%), *p-tert*-butylthiacalix[4] arene ($H_4TC4A$, Bide Co., Ltd., 99.0%), 2-hydroxysuccinic acid (Bide Co., Ltd., 95.0%), 5-mercapto-1-methyltetrazole (Bide Co., Ltd., 98.0%) $K_2SiF_6{:}Mn^{4+}$ (KSF, Zhanwanglong Co., Ltd. 99%), and $BaMgAl_{10}O_{17}{:}Eu^{2+}$ (BMA, Yaodexing Co., Ltd. 99%) were used as received without further purification.

**Synthesis of $\{[Eu_4(\mu_4\text{-}OH)(TC4A)_2(DMF)_6(CH_3OH)_3(HCOO)Cl_2]\}\cdot 0.33CH_3OH$ (1).** The mixture of $EuCl_3\cdot 6H_2O$ (0.86 g, 2.36 mmol), $H_4TC4A$ (0.28 g, 0.38 mmol) were dissolved in mixed solvent of MeOH and DMF (24 mL, v/v = 1 : 1). The solution was stirred at room temperature for 5 hours, and then triethylamine (TEA, 60 μL) was added. The solution sealed in a 50 mL Teflon-lined autoclave, which was kept at 140 °C for two days and then slowly cooled to 30 °C at about 3 °C $h^{-1}$. Colorless block-shaped crystals were isolated by filtration and then washed with 1 : 1 MeOH–DMF and dried in air (yield 50–60% based on Eu). FT-IR ($cm^{-1}$) (Fig. S1a†): 2969(m), 1644(m), 1607(s), 1451(s), 1359(m), 1311(s), 1267(s), 1248(s), 1098(m), 837(s), 746(s), 676(w), and 632(m).

**Synthesis of $\{[Tb_4(\mu_4\text{-}OH)(TC4A)_2(DMF)_6(CH_3OH)_3(HCOO)Cl_2]\}\cdot 0.66CH_3OH$ (2).** Compounds **2** were prepared in a procedure similar to that of **1**, except that $TbCl_3\cdot 6H_2O$ was utilized instead of $EuCl_3\cdot 6H_2O$. Yield: 70%.

**Synthesis of $\{[Gd_9(\mu_5\text{-}OH)_2\ (\mu_3\text{-}OH)_8(CH_3OH)_2(TC4A)_2(H_2O)_{24}]Cl_9\}\cdot 3.36$ DMF (3).** A mixture of $GdCl_3\cdot 6H_2O$ (0.2139 g, 0.58 mmol) and $H_4TC4A$ (0.691 g, 0.10 mmol) were dissolved in 6 mL of MeOH and DMF (1 : 1, v/v) and stirred at room temperature for 10 hours. The TEA (20 μL) was added in the solution and then enclosed in a 23 mL Teflon-lined autoclave. The Teflon-lined autoclave heated at 130 °C for two days and cooling to room temperature in one day, the white solution was filtrated and evaporated for 2 weeks. Colorless block crystals were isolated in a yield of 50%. FT-IR ($cm^{-1}$) (Fig. S1b†): 3391(w), 2948(m), 1575(s), 1450(s), 1361(s), 1360(m), 1509(m), 1093(w), 877(w), 647(w), 838(m), 740(w), 665(w), and 621(w).

**Synthesis of $\{[Tb_9(\mu_5\text{-}OH)_2(\mu_3\text{-}O)_8(OCH3)_9(TC4A)_2(H_2O)_{24}]Cl_9\}\cdot 2.6DMF$ (4) and $\{[Dy_9(\mu_5\text{-}OH)_2(\mu_3\text{-}OH)_8(OCH_3)_9(TC4A)_2(H_2O)_{24}]Cl_9\}\cdot 5.36DMF$ (5).** Compounds **4–5** were prepared in a procedure similar to that of **3**, except that $TbCl_3\cdot 6H_2O$ and $DyCl_3\cdot 6H_2O$ were utilized instead of $GdCl_3\cdot 6H_2O$. It is worth noting that, by volatilizing the filtrate of **2**, a small amount of **4** can also be obtained.

## Materials characterizations

Single crystals were mounted on a loop using viscous hydrocarbon oil. Data of **1–5** were collected at 200 K on a Bruker D8 CCD diffractometer equipped with an Oxford Cryosystem liquid $N_2$ device, using graphite-monochromated Mo-Kα radiation ($\lambda$ = 0.71073 Å) radiation. The structure **1–6** were solved by direct methods and refined by a full matrix least-squares technique based on $F^2$ using SHELXL-2018 within Olex2.[40,41] All non-hydrogen atoms were refined anisotropically. The hydrogen atoms of organic ligand were generated geometrically (C–H = 0.96 Å, N–H = 0.90 Å). The contribution of the disordered solvent molecules was subtracted from the reflection data by the SQUEEZE method as implanted in PLATON program.[42–45] Selected crystallographic data and structure determination parameters for complexes **1–5** are given in Table S1.† Selected bond lengths [Å] for **2** and **4** are given in Table S2.†

Powder X-ray diffraction (PXRD) data were recorded on a Rigaku miniflex 600 powder X-ray diffractometer (Cu Kα, $\lambda$ = 1.54184 Å) at room temperature. The IR spectrum was recorded (400–4000 $cm^{-1}$ region) on a Thermo Fisher Nicolet iS 50-IR spectrophotometer in the range of 4000–400 $cm^{-1}$. Thermogravimetric analyses (TGA) were carried out on a TGA-50 thermogravimetric analyzer from 30 to 800 °C in an argon atmosphere with a heating rate of 5 °C $min^{-1}$.

The emission (EM) spectra, excitation (EX) spectra were measured at room temperature using a spectrometer (FLS 980, Edinburgh Instruments) equipped with both continuous (450 W) and microsecond pulsed xenon (Xe) lamps with the detection of emission spectra out to 2100 nm and time-correlated single-photon counting lifetime measurements as short as 30 ps. Measurement of emission spectra using excitation at the strongest excitation wavelength, 396 nm for **1** and 350 nm for **2** and **4**. To investigate the PL thermal stability at 298–573 K, the samples were placed on a thermal stage (77–873 K, THMS 600, Linkam Scientific Instruments), and a fiber-coupled spectrometer (QE 65000, Ocean Optics) was used to record the emission spectra of the sample under excitation by 350 nm light. Each temperature dependent spectrum was collected after the target temperature was maintained for no less than 5 min. The photoluminescence decay spectra were collected on the same spectrofluorometer with an excitation wavelength of 350 nm as the lighting source. Quantum efficiency were measured at room temperature with an FLS 980 spectrometer. Quantum efficiency, defined as the ratio between the number of photons emitted by the $Ln^{3+}$ ion to the number of those absorbed, could be calculated by means of eqn (1):[46]

$$\eta = A_R/(A_R + A_{NR}), \quad (1)$$

where $A_R$ and $A_{NR}$ are the non-radiative transition probabilities.

## Results and discussion

### Crystal structure

The tetranuclear $\{Ln_4\}$ clusters in **1–2** are obtained by reacting $LnCl_3 \cdot 6H_2O$ (Ln = Eu/Tb) with $H_4TC4A$ in a mixed solution of ethanol and DMF. Single-crystal X-ray diffraction shows that the two compounds are isostructural. As a representative example, we only illustrate the structural features of **2** in details. In the structure, the four trivalent cation $Tb^{3+}$ atoms are nine-fold coordinated with O, S, and Cl atoms to give $[TbO_6S_2Cl]$ and $[TbO_7S_2]$ polyhedra (Fig. 1a). Two $[TbO_6S_2Cl]$ polyhedra and two $[TbO_7S_2]$ polyhedra are further connected by eight $\mu_2$-O and one $\mu_4$-OH (Table S3†) to give the $[Tb_4(\mu_2\text{-}O_{phenoxo})_8(\mu_4\text{-}OH)S_8Cl_2O_6]$ (Fig. 1b) polynuclear cluster with the square $[Tb_4(\mu_4\text{-}OH)]$ core (Fig. 1c). The Tb⋯Tb distances on the edge (linked by $O_{phenoxo}$) and the diagonal (linked by $\mu_4$-OH) of the $[Tb_4(\mu_4\text{-}OH)]$ core are 3.563–3.583 Å and 4.922–5.966 Å, respectively. The $[Tb_4(\mu_2\text{-}O_{phenoxo})_8(\mu_4\text{-}OH)S_8Cl_2O_6]$ clusters are capped by two TC4A ligands in a tail-to-tail mode to form two slightly different sandwich-like cluster structures, namely $[Tb_4(\mu_4\text{-}OH)(CH_3\text{-}OH)(TC4A)_2(DMF)_2(HCOO)_2Cl_2]^-$ (A) and $[Tb_4(\mu_4\text{-}OH)(TC4A)_2(\text{-}DMF)_6Cl_2]^+$ (B) (Fig. 1d). These two types of clusters are arranged alternately in the *bc* plane, as shown in the structure of **2** (Fig. 1e).

On the other hand, by evaporating the reaction solution after the solvothermal process, we obtained nonanuclear clusters (**3–5**). **3–5** crystallize in the tetragonal space group *P*4/*nnc* with similar structures so we only describe the structure of **4** in details here. The nonanuclear cluster in **4** also exhibits a sandwich-like structure, with a $C_4$ axis passing through the central $Tb^{III}$ atom. In this structure, the trivalent $Tb^{3+}$ cations are nine-fold and ten-fold coordinated with O and S atoms to give the $[TbO_8S]$ and $[TbO_{10}]$ polyhedra, respectively (Fig. 2a). Eight $[TbO_8S]$ and one $[TbO_{10}]$ polyhedra are further connected by $\mu_3$-OH and $\mu_5$-OH (Table S3†) to form the $[Tb_9(\mu_2\text{-}O_{phenoxo})_8(\mu_3\text{-}OH)_8(\mu_5\text{-}OH)_2S_8O_{27}]$ cluster (Fig. 2b) with a hourglass-like $[Tb_9(\mu_3\text{-}OH)_8(\mu_5\text{-}OH)_2]$ core (Fig. 2c). The $[Tb_9(\mu_5\text{-}OH)_2(\mu_3\text{-}OH)_8]$ core consists of two square $\{Tb_4\}$ units that are connected by one $Tb^{3+}$ ion *via* eight $\mu_3$-OH groups. The two planar $\{Tb_4\}$ units are rotated by about 45° from

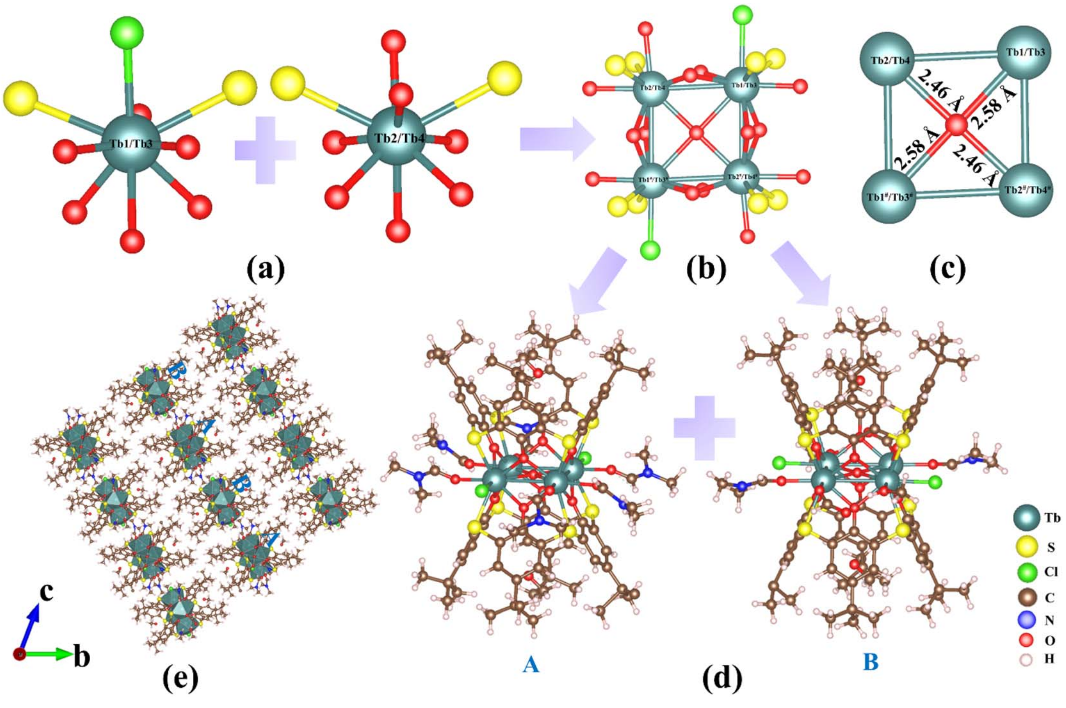

Fig. 1 (a) $[TbO_6S_2Cl]$ and $[TbO_7S_2]$ polyhedra; (b) $[Tb_4(\mu_2\text{-}O_{phenoxo})_8(\mu_4\text{-}OH)S_8Cl_2O_6]$ polyhedron. (c) Square core $[Tb_4(\mu_4\text{-}OH)]$ of **2**; (d) sandwich-like cluster molecules A and B of **2**; (e) stacking motif of **2** in the ac plane. Solvent molecules are removed for clarity.

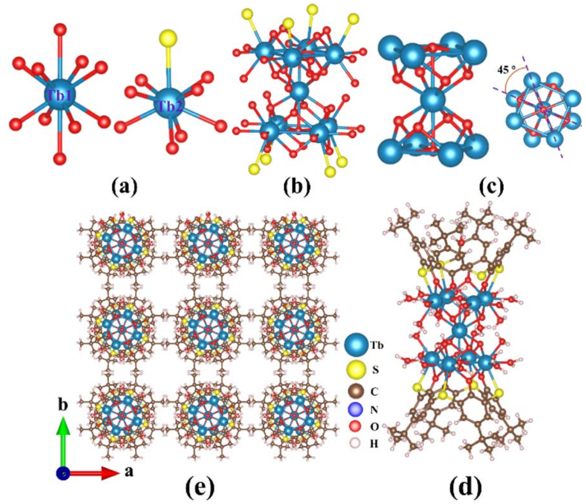

Fig. 2 (a) $[TbO_8S]$ and $[TbO_{10}]$ polyhedra; (b) $[Tb_9(\mu_2\text{-}O_{phenoxo})_8(\mu_3\text{-}OH)_8(\mu_5\text{-}OH)_2S_8O_{27}]$ polyhedron. (c) Hourglass-like $[Tb_9(\mu_3\text{-}OH)_8(\mu_5\text{-}OH)_2]$ core; (d) sandwich-like cluster structure of **4**; (e) 3D structure of **4**.

each other, which likely reduces the charge repulsion between $Tb^{3+}$ ions and stabilize the structure. Similar to the tetranuclear $\{Ln_4\}$ clusters in **1–2**, the hourglass-like nonanuclear core $[Tb_9(\mu_5\text{-}OH)_2(\mu_3\text{-}OH)_8]$ is also capped by two thiacalix[4]arene ligands in a tail-to-tail fashion to form a sandwich-like entity.

### Possible cluster-assembling pathways

Although the coordination sites on $H_4TC4A$ favor to support the lanthanide nanoclusters according to the hard–soft-acid–base principle,[47] the bulky skeleton of $H_4TC4A$ may introduce uncertainty during the assembly of high nuclear clusters, especially under the presence of labile lanthanide cations. Indeed, based on a survey of the Cambridge Crystallographic Data Centre (CCDC, Version 2020.3.0), large $H_4TC4A$-supported homometallic clusters that have been reported are all based on transition metal cations, such as the wheel-like $\{Ni_{18}\}$,[33] $\{Ag_{88}\}$[36] cluster, the Johnson-type ($J_{17}$) hexadecahedron $\{Ni_{40}\}$[35] cage, and the nanosphere-like $\{Co_{32}\}$[32] cluster. $H_4TC4A$-protected homometallic lanthanide nanoclusters is less reported – $[Ln_4^{III}(TC4A)_2(\mu_4\text{-}OH)Cl_3(CH_3OH)_2(H_2O)_3]$ (Ln = Dy, Tb)[37] and $[Ln_5(\mu_5\text{-}OH)(\mu_3\text{-}OH)_4(TC4A)(acac)_6]$ (Ln = Dy, Ho, Er)[38] are the only two examples reported, as far as we know. The structure of $[Ln_4^{III}(TC4A)_2(\mu_4\text{-}OH)Cl_3(CH_3OH)_2(H_2O)_3]$ (Ln = Dy, Tb) has a similar tetranuclear cluster core $[Tb_4(\mu_4\text{-}OH)]$ as **2** but is crystallized in a different space group. The $[Ln_5(\mu_5\text{-}OH)(\mu_3\text{-}OH)_4(TC4A)(acac)_6]$ cluster shows a gyro-like structure with a pyramidal $[Ln_5(\mu_5\text{-}OH)(\mu_3\text{-}OH)_4]$ core (Fig. S2a and b†). In this regard, the $\{Ln_9\}$ clusters in **3–5**, with the hourglass-like core $[Ln_9(\mu_5\text{-}OH)_2(\mu_3\text{-}OH)_8]$, are the largest homometallic lanthanide cluster supported by $H_4TC4A$ ligands, although similar core structure has been seen in 2-(hydroxymethyl)pyridine and β-diketonate ligands supported structures.[48,49]

The above-mentioned homometallic lanthanide cluster structures ($\{Ln_4\}$, $\{Ln_5\}$, and $\{Ln_9\}$) appear to be highly related, which might provide insights into the assembling process during the solution synthesis. We speculate the following pathway based on these structures (Fig. 3): first, the deprotonated $H_4TC4A$ ligands combine with four $Ln^{3+}$ ions to form the single TC4A-capped tetranuclear building units (tetra-BU) with the $[Ln_4(\mu_4\text{-}OH)]$ core (Fig. 3a–c); second, depending on the regulation of different template anions ($Cl^-$ and $acac^-$), the tetra-BU either coordinates with an adjacent free $TC4A^{4-}$ ligand to form the sandwich-like double-capped $\{Ln_4\}$ clusters (Fig. 3d) or condenses with one $Ln^{3+}$ ions to obtain the inverted pyramid-like $\{Ln_5\}$ clusters (Fig. 3e), leading to the two major cluster

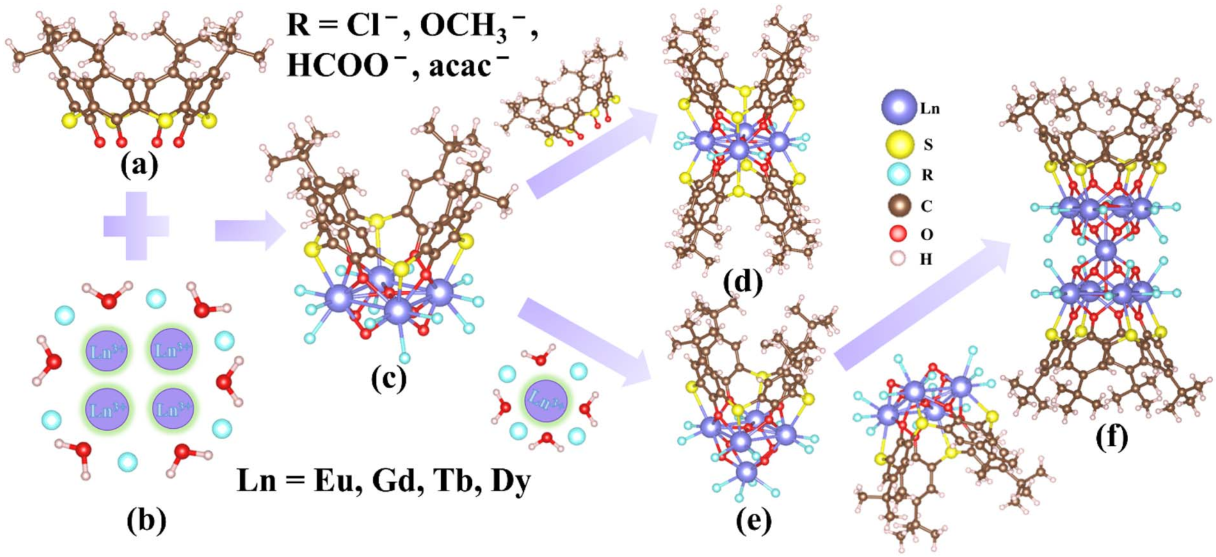

Fig. 3 Proposed assembling process of $H_4TC4A$-capped rare-earth cluster. (a) Structure of $H_4TC4A$ ligand; (b) coordination environment of rare earth ions in solution; (c) $[Ln_4(\mu_4\text{-}OH)(TC4A)]$ tetra-BU; (d) sandwich-like $H_4TC4A$-supported $\{Ln_4\}$ clusters; (e) inverted pyramid-like $H_4TC4A$-supported $\{Ln_5\}$ clusters; (f) sandwich-like $H_4TC4A$-supported $\{Ln_9\}$ clusters.

structures that have been reported previous; finally, during the evaporation process, the {$Ln_5$} clusters (with the pyramidal [$Ln_5(\mu_5\text{-OH})(\mu_3\text{-OH})_4$] core) may further condense with a nearby tetra-BU by forming four $\mu_3$-OH bridges, resulting in the double-capped {$Ln_9$} clusters in **3–5** (Fig. 3f). This might be a possible explanation for why the {$Ln_9$} clusters could be obtained by evaporating the reaction solution of {$Ln_4$} clusters for about two weeks. The {$Ln_5$} clusters likely exist as an intermediate substance that cannot be isolated during the synthetic process of {$Ln_4$} or {$Ln_9$}. Crystallization of {$Ln_5$} clusters can be achieved by using $Ln(acac)_3 \cdot 2H_2O$ as the reactant.

## Effects of the core structure on the luminescent properties

To investigate the luminescent properties of the double thiacalix[4]arene-capped **1–5** clusters, we synthesize polycrystalline samples of **1–5**. Their PXRD patterns are shown in Fig. S3a and b.† The experimental patterns show good consistency with the simulated ones, confirming the good phase purity of the polycrystalline samples.

The photoluminescence properties of **1**, **2**, and **4** are analyzed at ambient temperature. When monitored at the strongest excitation, the emission spectra of **1** (Fig. 4a) and **2** (or **4**) (Fig. 4b and S4†) show clear distinction between 450 and 750 nm, which is closely related to the different transition energy of $Eu^{3+}$ and $Tb^{3+}$. With the 396 nm excitation, the emission spectrum of tetranuclear cluster **1** exhibits the typical emission features of $Eu^{3+}$ from the excited $^5D_0$ energy level to the ground state $^7F_j$ ($j = 1, 2, 3$, and 4) multiplets. The maximum emission intensity is observed at 614 nm, which corresponds to the $^5D_0 \rightarrow {}^7F_2$ electric-dipole transition of $Eu^{3+}$ (Fig. 4a and S4a†).[50] Based on the calculation, cluster **1** shows a relatively lower quantum yield (QY) of ~5%.

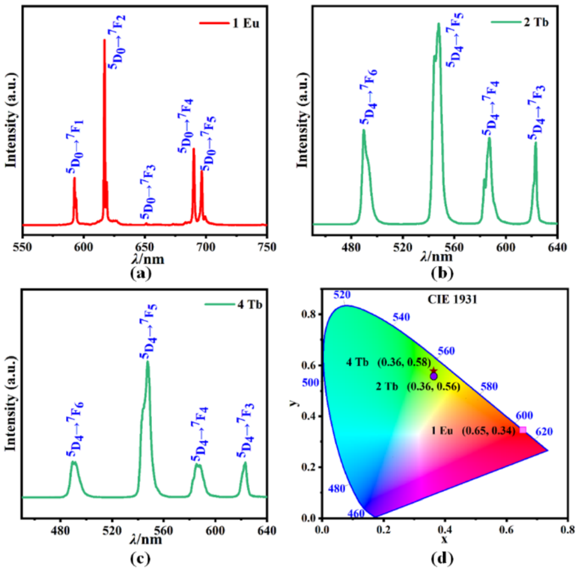

Fig. 4 (a) Emission spectra of **1**; (b) emission spectra of **2**; (c) emission spectra of and **4**; (d) CIE chromaticity coordinate diagram of the **1**, **2**, and **4**.

On the other hand, the tetranuclear cluster **2** and nonanuclear cluster **4** powder products with $Tb^{3+}$ are of white color under sunlight and emit green light under the 350 nm UV illumination, which might suggest similar spectroscopic properties. For both compounds, the emission bands (Fig. 4b, c and S4b, c†) consist of transitions from $^5D_4$ levels to its $^7F_J$ ($J = 6, 5, 4$, and 3). The emission bands at 491, 547, 586, and 623 nm correspond to the $^5D_4 \rightarrow {}^7F_6$, $^5D_4 \rightarrow {}^7F_5$, $^5D_4 \rightarrow {}^7F_4$, and $^5D_4 \rightarrow {}^7F_3$ transitions, respectively.[51] Among these peaks, the $^5D_4 \rightarrow {}^7F_5$ transition exhibits the highest intensity, which leads to the predominant green color. It appears that the cluster core structure does not affect the luminescent color significantly.

The CIE 1931 (Commission International d'Eclairage) diagram is a universal method for achieving possible colors by combining three primary colors, which has been extensively used for the targeted tuning on the emission wavelength and intensity. The emission spectra of **1**, **2**, and **4** are converted into the $x$ and $y$ coordinates in the CIE chromaticity diagram, as presented in Fig. 4d. The chromaticity coordinates ($x$, $y$) are found to be (0.65, 0.34), (0.36, 0.56), and (0.36, 0.58) for **1**, **2**, and **4**, respectively. The overall emission of the three samples is evaluated in terms of standard chromaticity diagram CIE, which can be easily seen to be red for **1**, green for **2** and **4**. These results are close to those obtained from the reported Ln-containing compounds.[9,11,16]

Nevertheless, although similar in emission colors, it is worth noting that the emission intensity of **2** is about twice as strong as that of **4** (Fig. S4d†), when monitored at the same test conditions. Cluster **2** also exhibit much higher quantum yield (QY) (~65%) than that of **4** (~30%). This is likely attributed to their different cluster structures. Although both cluster **2** and cluster **4** are double-capped by two TC4A ligands, cluster **4** exposes more terminal water molecules and $\mu_3$-OH bridges on the equatorial positions than **2**. It is well-known that the coordinated water molecules can lead to vibrational quenching of the rare-earth emission centers, especially when these water molecules have more freedom to rotate or stretch.[52] In **4**, the terminal water molecules and $\mu_3$-OH bridges on the {$Ln_9$} clusters are not involved in a strong hydrogen bonding network and therefore contribute easily to vibrational quenching.[9] In contrast, terminal ligands such as $-OCH_3$, $-ON(CH_3)_2$, and –TC4A protect the central [$Tb_4(\mu_4\text{-OH})$] core in **2**, which effectively prevents the vibrational quenching and enhances the QY of **2**.

The room-temperature photoluminescence decay curves of the polycrystalline powder of **1**, **2**, and **4** are also characterized, shown in Fig. S5.† The decay curves can be fitted with a double-exponential decay model, represented by the following eqn (2):[53]

$$I = A_1 \exp(-t/\tau_1) + A_2 \exp(-t/\tau_2), \tag{2}$$

where $I$ is the emission intensity at a given time $t$, $A_i$ and $\tau_i$ ($i = 1$, 2) are the contributing amplitude and lifetime, respectively, of the corresponding decay processes. Based on the fitting results, the corresponding lifetime values of **1**, **2**, and **4** are as follows: $\tau_1 = 6.36 \times 10^4$ ns and $\tau_2 = 2.59 \times 10^5$ ns for **1**; $\tau_1 = 4.98 \times 10^5$ ns and $\tau_2 = 1.36 \times 10^6$ ns for **2**; $\tau_1 = 4.92 \times 10^5$ ns and $\tau_2 = 1.01 \times$

$10^6$ ns for **4**. Hence, the average decay time ($\tau^*$) of **1**, **2**, and **4** can be calculated as $5.22 \times 10^4$ ns, $1.34 \times 10^6$ ns, and $1.00 \times 10^6$ ns (Table S4†), respectively, based on eqn (3):[53]

$$\tau^* = (A_1\tau_1^{\,2} + A_2\tau_2^{\,2})/(A_1\tau_1 + A_2\tau_2) \tag{3}$$

These results are also comparable to other reported $\text{Ln}^{\text{III}}$ complexes. It is worth pointing out that **2**, and **4** do not show significant difference in the decay time.

Besides these basic luminescent properties, it is also important to investigate the luminescent stability of these compounds when exposed to moisture and high temperature. For example, theoretical and experimental studies have proven that solvent molecules (*e.g.* $H_2O$) will enter the lattice and trigger hydrolysis and decomposition. These deteriorations not only destroy the crystal structure of the material, but also significantly enhances the vibrational quenching on the emission centers.[54–58] Therefore, the luminescent stability of **2** and **4** against moisture are characterized in details first.

We add the polycrystalline sample of **2** (tetranuclear double-capped cluster $\{Ln_4\}$) and **4** (nonanuclear double-capped cluster $\{Ln_9\}$) to water and let them sit for ten days. The two samples show very different behaviors: compound **2** is hydrophobic and floats on surface of water (Fig. 5a), while **4** sinks to the bottom of the bottle and partially dissolves over time (Fig. 5b). Meanwhile, the luminescent intensity of **2** maintains almost at the same level (96.5% of initial luminescent intensity) before and after soaking in water (Fig. 5c). However, the luminescent intensity of **4** decreases by more than 40% after ten days (Fig. 5d). The SEM images of the polycrystalline sample of **2** and **4** after soaking are shown in Fig. S6.† The result reveals that **2** is capable of maintaining its crystalline morphology (Fig. S6a†), with the surface of crystals remaining smooth (Fig. S6b†) after immersed in water for two weeks. In contrary, the crystalline particles of **4** break into smaller pieces after the soaking (Fig. S6c†), with the surface of the crystal significantly roughened, indicating dramatic deterioration (Fig. S6d†). The XRD patterns of the polycrystalline sample of **2** and **4** after soaking are shown in Fig. S7.† As we can see, no significant changes are observed in the XRD pattern of **2**, demonstrating its superior water stability. On the other hand, although **4** basically maintains its crystal structure, it is clear that unknown phases have been generated during the soaking period.

To further evaluate the hydrophobic properties of **2** and **4** in detail, static water contact angles (CA) measurements are performed with a water droplet (10 μL) on tableted samples. The average CA of **2** researches 126° (Fig. 5e), higher than that of **4** (101°, Fig. 5f). The difference in hydrophobicity between **2** and **4** can be explained based on the structural difference, especially the differences on polynuclear cluster cores. The luminescent center of **2** is mostly wrapped by hydrophobic $-OCH_3$, $-ON(CH_3)_2$, and –TC4A groups, which create a "molecular encapsulation" effect that protects the tetranuclear $[Tb_4(\mu_4\text{-}O)]$ core from moisture invasion. This "molecular encapsulation"

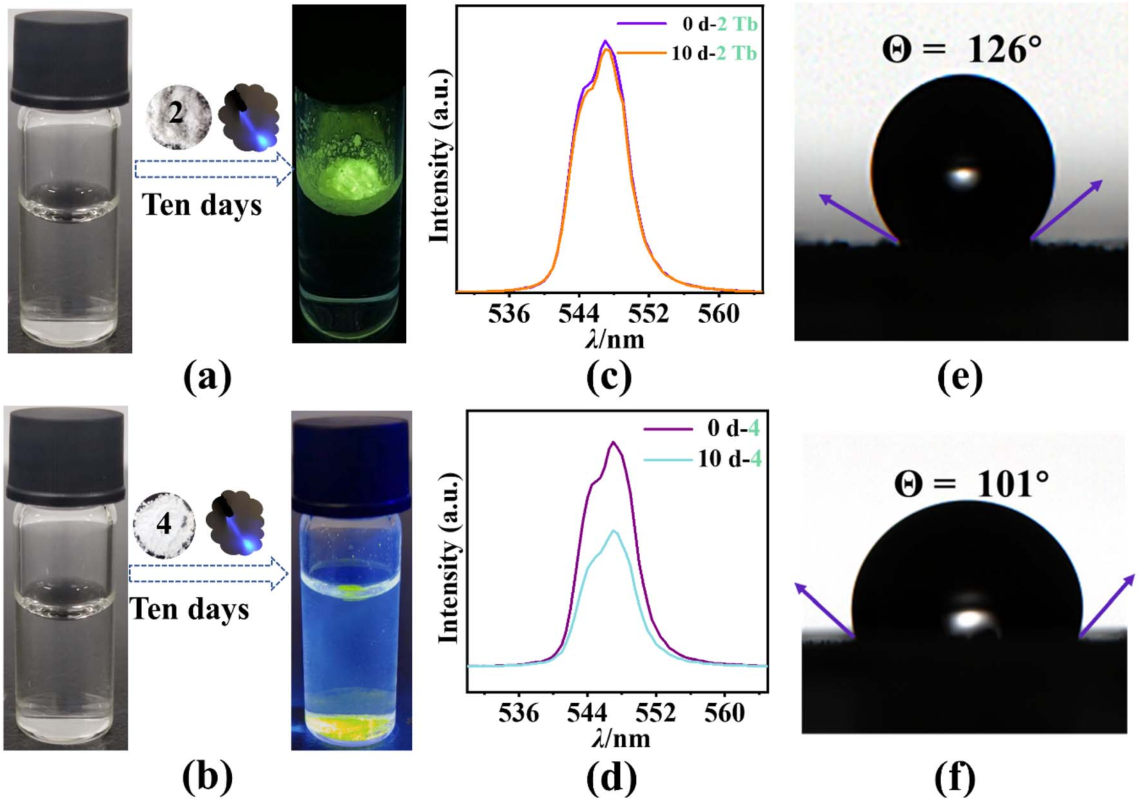

Fig. 5 Water-resistant test. The appearance of **2** (a) and **4** (b) in water and; emission spectra of **2** (c) and **4** (d) water for different periods; static water contact angles measurements of **2** (e) and **4** (f).

effect enables cluster **2** in exhibiting highly stable photoluminescence even after soaking in the water for a long period. Compared with **2**, although both axial positions of the luminescence center in **4** (the nonanuclear $[Tb_9(\mu_5\text{-}OH)_2(\mu_3\text{-}O)_8]$ core), are covered by the hydrophobic $TC4A^-$ ligands, a large number of hydrophilic groups (*e.g.* terminal water molecules and hydroxyl bridges) are located in the equatorial direction. These hydrophilic groups allow the solvent to attack on the luminescent centers and significantly affect the luminescence stability. In addition, compared with the traditional encapsulation method (*e.g.* compositing, surface engineering, and device encapsulation, *etc.*), the one-step synthesis of phosphor **2** demonstrates a facile synthetic route towards intrinsic protection against moisture degradation.

In additional to moisture stability, the thermal stability of phosphors is another important aspect that is critical for practical applications (the operation temperature of an LED device can reach 150 °C).[59–62] Before analyzing the luminescent stability at high temperature, we first look at the structural stability of **2** and **4** at elevated temperatures by conducting thermogravimetry analysis (TGA). The TGA curve of **2** do not show significant weight loss until 327 °C, which likely because of the decomposition of ligands (Fig. S9a†). To further confirm the structural stability of **2** at high temperature, we collect the powder XRD patterns of **2** after annealing it at 100, 200, 250, and 300 °C for 24 h. As shown in Fig. S9b,† no significant changes are observed in the XRD patterns even when the annealing temperature reaches above 300 °C, demonstrating the superior thermal stability of **2**. In the contrary, we observe significant weight loss at 30 °C and 219 °C on **4** (Fig. S9c†), likely indicating structural changes at high temperature. Indeed, significant changes can be observed in the XRD patterns after annealing the polycrystalline samples of **4** over 60 °C (Fig. S9d†). It is clear that, although both tetranuclear cluster **2** and nonanuclear cluster **4** have similar double-capped structures, cluster **2** exhibits much higher thermal stability than cluster **4**. Looking at the polynuclear core structure, we postulate that the large number of water molecules and hydroxyl bridges on the nonanuclear $[Tb_9(\mu_5\text{-}OH)_2(\mu_3\text{-}O)_8]$ core may likely undergo dehydration under heating, which leads to the collapsing of the nonanuclear cluster structure in **4**.[63–65]

Because of the superior structural stability, we further characterize the luminescent stability of **2** under higher temperature and extended UV exposure. First, we conduct the solid-state temperature-dependent photoluminescence measurements from 25 to 275 °C under 350 nm excitation on **2**. The results are summarized in Fig. 6a. As we can see, **2** exhibits highly stable luminescence when the temperature increases from 25 °C to 150 °C, with the luminescence intensity remaining as high as 92.1% of its initial value at 150 °C. When the temperature increases to 200 °C, the luminescence intensity still maintains at 70.0% of its room temperature value. More importantly, no shift in the peak positions is observed over the entire temperature range from 25 °C to 300 °C, which is consistent with excellent structural stability of **2**. As shown in Fig. 6b, the emission intensity of **2** is highly stable, with the change of less than 8.0% and 30.0% at 150 °C and 200 °C, respectively. A straightforward parameter that reflects the thermal stability of luminescence is $T_{50}$, defined as the temperature at which the emission intensity has been quenched to 50% of its initial value. The $T_{50}$ of **2** reaches 236 °C, indicating that it has the ability to withstand high operating temperatures. It is worth pointing out that the luminescence stability of **2** at high temperature is even better than that of some commercial phosphors (*e.g.* $(Ba,Sr)_2SiO_4:Eu^{2+}$, with 41% emission intensity loss at 200 °C).[66,67]

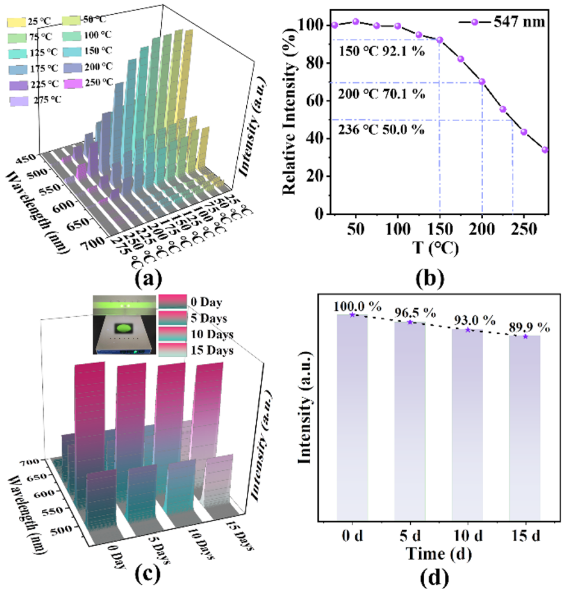

Fig. 6 (a) Photoluminescence emission spectra of compound **2** measured at the temperatures from 25 °C to 300 °C under 350 nm excitation; (b) the relationship between the integrated emission intensity and the testing temperatures; (c) photoluminescence emission spectra of **2** measured at different UV-exposure time; (d) relationship between the relative emission intensity and the UV-exposure time.

Second, for evaluating the luminescent stability of **2** under extended UV exposure, we leave it under continuous 365 nm UV illumination for 15 days. In Fig. 6c and d, we observe that the emission intensity of **2** exhibits only minor changes before and after the 15 days UV illumination. After the 15 days UV exposure period (Fig. 6c), the emission intensity remains as high as 89.9% of the initial value (Fig. 6d). It is clear that **2** also possesses great luminescent stability under UV exposure.

The excellent thermal stability and radiation stability of **2** may be caused by two reasons. First, the TC4A coordinates to the $[Tb_4(\mu_4\text{-}OH)]$ core *via* multiple Tb–O and Tb–S bonds, creating a highly stable emission center. Second, the $[Tb_4(\mu_4\text{-}OH)]$ core connects to terminal $-OCH_3$, $-OCHN(CH_3)_2$, $Cl^-$, and $HCOO^-$ groups in the equatorial directions. The decomposition of terminal groups, although might happen at elevated temperature, do not change the core structure of the luminescent centers. With the excellent structural stability contributed by the ligand and terminal groups, the chemical environment surrounding the luminescent centers maintains intact even under the harsh heating and UV radiation, which is highly desired for achieving stable luminescence.

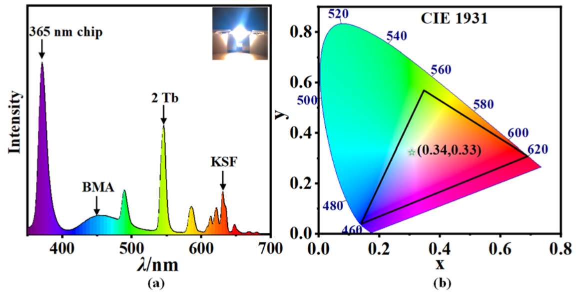

Fig. 7 (a) PL spectra of a working WLED (inset) based on the crystalline powder of **2**, KSF, and BMA on an InGaN chip; (b) the CIE color coordinates of the WLED device.

All of the above tests show that **2** exhibit strong and sharp emission bands, good thermal stability, and excellent hydrophobic properties, demonstrating great potential as a green phosphor. In the following section, we adopt **2** in an prototype LED device for evaluating its potential for applications.

### Light-emitting diodes (LEDs) fabrications

We fabricate a while-light LED device with **2**, in combination with the commercially available KSF and BMA phosphors.

Powders of **2**, KSF, and BMA are mixed with AB glue and then smeared on an InGaN blue chip, which is further cured at 120 °C for 2 h to obtain the white-LED (w-LED) (Fig. 7a inset). The emission spectrum (Fig. 7a) of the w-LED contains the characteristic emissions of the three phosphors, with **2** as the major source of green emission. CIE coordinate of the white w-LED is determined to be (0.34, 0.33) with a 74.3% color gamut range (NEST standard) (Fig. 7b). During the continuous operation, this prototype w-LED perform stably without apparent intensity attenuation for more two weeks. The luminance efficiency of w-LED device obtained using **2** is 33 lm $W^{-1}$, which is better than that of traditional commercial gas-filled incandescent lamps (12–19 lm $W^{-1}$). This demonstrates the potential of **2** as a new phosphor choice for practical w-LED applications.

## Conclusion

In conclusion, two types double *p-tert*-butylthiacalix[4]arene ($H_4TC_4A$) capped lanthanide-oxo cluster compounds, *i.e.* the tetranuclear $\{[Ln_4(\mu_4\text{-}OH)(TC4A)_2(DMF)_6(CH_3OH)_3(HCOO)Cl_2]\}\cdot xCH_3OH$ (Ln = Eu (**1**), Tb (**2**); $x$ = 0–1) clusters and the nonanuclear $\{[Ln_9(\mu_5\text{-}OH)_2(\mu_3\text{-}OH)_8(OCH_3)(TC4A)_2(H_2O)_{24}Cl_9]\}\cdot xDMF$ (Ln = Gd (**3**), Tb (**4**), Dy (**5**); $x$ = 2–6) clusters, are synthesized. The formation of these clusters may undergo a $\{Ln_4\}$–$\{Ln_5\}$–$\{Ln_9\}$ transition process, resulting in the $\{Ln_9\}$ clusters with the hourglass-like $[Ln_9(\mu_5\text{-}OH)_2(\mu_3\text{-}OH)_8]$ core. The $\{Ln_9\}$ clusters are the largest homometallic $H_4TC4A$-supported lanthanide-oxo clusters. We find that the polynuclear core structure dictates the luminescent properties of the cluster compounds, with the $\{Ln_4\}$ core exhibiting superior performance over the $\{Ln_9\}$ core. Photoluminescence tests show that **2** exhibits bright green emission (with the CIE chromaticity coordinates of (0.36, 0.58), high luminescent emission intensity, and large quantum yield (~65%). More importantly, **2** demonstrates excellent long-term luminescent stability against moisture, elevated temperature, and UV exposure. A white-LED device is constructed to evaluate the potential of **2** for practical applications and the device demonstrates stable operation during the long-term test. Our work provides a new alternative for achieving structurally stable lanthanide complexes by exploiting the coordination chemistry of *p-tert*-butylthiacalix[4]arene ($H_4TC4A$) with careful design on the polynuclear core structure.

## Conflicts of interest

There are no conflicts to declare.

## Acknowledgements

This work was supported by NSF of China (21871262 and 21901242), NSF of Fujian Province (2020J05080), NSF of Xiamen (3502Z20206080), the Key Research Program of the Chinese Academy of Sciences (ZDRW-CN-2021-3-3), the Youth Innovation Promotion Association CAS (2021302), Fujian Science & Technology Innovation Laboratory for Optoelectronic Information of China (2021ZR110), and the Recruitment Program of Global Youth Experts.

## References

1 I. Colliard, J. C. Brown, D. B. Fast, A. K. Sockwell, A. E. Hixon and M. Nyman, Snapshots of $Ce_{70}$ Toroid Assembly from Solids and Solution, *J. Am. Chem. Soc.*, 2021, **143**, 9612–9621.
2 L. Qin, Y. Z. Yu, P. Q. Liao, W. Xue, Z. Zheng, X. M. Chen and Y. Z. Zheng, A "Molecular Water Pipe": A Giant Tubular Cluster $\{Dy_{72}\}$ Exhibits Fast Proton Transport and Slow Magnetic Relaxation, *Adv. Mater.*, 2016, **28**, 10772–10779.
3 X. Y. Zheng, X. J. Kong, Z. P. Zheng, L. S. Long and L. S. Zheng, High-Nuclearity Lanthanide-Containing Clusters as Potential Molecular Magnetic Coolers, *Acc. Chem. Res.*, 2018, **51**, 517–525.
4 X. M. Luo, Z. B. Hu, Q. Lin, W. Cheng, J. P. Cao, C. H. Cui, H. Mei, Y. Song and Y. Xu, Exploring the Performance Improvement of Magnetocaloric Effect Based Gd-Exclusive Cluster $Gd_{60}$, *J. Am. Chem. Soc.*, 2018, **140**, 11219–11222.
5 H. L. Wang, T. Liu, Z. H. Zhu, J. M. Peng, H. H. Zou and F. P. Liang, A series of dysprosium clusters assembled by a substitution effect-driven out-to-in growth mechanism, *Inorg. Chem. Front.*, 2021, **8**, 2136–2143.
6 X. Y. Zheng, Y. H. Jiang, G. L. Zhuang, D. P. Liu, H. G. Liao, X. J. Kong, L. S. Long and L. S. Zheng, A Gigantic Molecular Wheel of $\{Gd_{140}\}$: A New Member of the Molecular Wheel Family, *J. Am. Chem. Soc.*, 2017, **139**, 18178–18181.
7 W. M. Wang, Z. L. Wu, Y. X. Zhang, H. Y. Wei, H. L. Gao and J. Z. Cui, Self-assembly of tetra-nuclear lanthanide clusters *via* atmospheric $CO_2$ fixation: interesting solvent induced structures and magnetic relaxation conversions, *Inorg. Chem. Front.*, 2018, **5**, 2346–2354.

8 A. V. Virovets, E. Peresypkina and M. Scheer, Structural Chemistry of Giant Metal Based Supramolecules, *Chem. Rev.*, 2021, **121**, 14485–14554.

9 D. T. Thielemann, A. T. Wagner, E. Rösch, D. K. Kölmel, J. G. Heck, B. Rudat, M. Neumaier, C. Feldmann, U. Schepers, S. Bräse and P. W. Roesky, Luminescent Cell-Penetrating Pentadecanuclear Lanthanide Clusters, *J. Am. Chem. Soc.*, 2013, **135**, 7454–7457.

10 X. J. Lv, X. L. Zhao, Q. X. Zhao, Q. Zheng and W. M. Xuan, Cerium-oxo clusters for photocatalytic aerobic oxygenation of sulfides to sulfoxides, *Dalton Trans.*, 2022, **51**, 8949–8954.

11 X. Y. Li, Y. Jing, J. Zheng, H. Ding, Q. Li, M. H. Yu and X. H. Bu, Two Luminescent High-Nuclearity Lanthanide Clusters $Ln_{48}$ ($Ln = Eu$ and Tb) with a Nanopillar Structure, *Cryst. Growth Des.*, 2020, **20**, 5294–5301.

12 Y. F. Jiang, K. Zheng, Z. Q. Liu, X. B. Yu, Q. R. Yang, T. Tang and C. H. Zeng, Synthesis of Two New Dinuclear Lanthanide Clusters and Visual Bifunctional Sensing Devices Based on the Eu Cluster, *Adv. Opt. Mater.*, 2021, **10**, 2102267.

13 R. Karashimada and N. Iki, Thiacalixarene assembled heterotrinuclear lanthanide clusters comprising $Tb^{III}$ and $Yb^{III}$ enable *f–f* communication to enhance $Yb^{III}$-centred luminescence, *Chem. Commun.*, 2016, **52**, 3139–3142.

14 H. F. Chen, X. P. Yang, D. M. Jiang, D. Schipper and R. A. Jones, NIR luminescence for the detection of metal ions and nitro explosives based on a grape-like ninenuclear Nd(III) nanocluster, *Inorg. Chem. Front.*, 2019, **6**, 550–555.

15 R. Chen, Z. F. Hong, Y. R. Zhao, H. Zheng, G. J. Li, Q. C. Zhang, X. J. Kong, L. S. Long and L. S. Zheng, Ligand-Dependent Luminescence Properties of Lanthanide–Titanium Oxo Clusters, *Inorg. Chem.*, 2019, **58**, 15008–15012.

16 J. H. Zheng, Q. J. Cheng, S. Q. Wu, Z. Q. Guo, Y. X. Zhuang, Y. J. Lu, Y. Li and C. Chen, An efficient blue-emitting $Sr_5(PO_4)_3Cl:Eu^{2+}$ phosphor for application in near-UV white light-emitting diodes, Chen, *J. Mater. Chem. C*, 2015, **3**, 11219–11227.

17 A. Beeby, I. M. Clarkson, R. S. Dickins, S. Faulkner, D. Parker, L. Royle, A. S. de Sousa, J. A. G. Williams and M. Woods, Non-radiative deactivation of the excited states of europium, terbium and ytterbium complexes by proximate energy-matched OH, NH and CH oscillators: an improved luminescence method for establishing solution hydration states, *J. Chem. Soc., Perkin Trans. 2*, 1999, 493–504.

18 X. Qin, X. W. Liu, W. Huang, M. Bettinelli and X. G. Liu, Lanthanide-Activated Phosphors Based on 4f-5d Optical Transitions: Theoretical and Experimental Aspects, *Chem. Rev.*, 2017, **117**, 4488–4527.

19 T. Y. Gao, W. D. Zhuang, R. H. Liu, Y. H. Liu, C. P. Yan and X. X. Chen, Design of a Broadband NIR Phosphor for Security-Monitoring LEDs: Tunable Photoluminescence Properties and Enhanced Thermal Stability, *Cryst. Growth Des.*, 2020, **20**, 3851–3860.

20 P. F. Zhu, Q. Zhu, H. Y. Zhu, H. F. Zhao, B. Chen, Y. Zhang, X. Wang and W. Di, Effect of $SiO_2$ Coating on Photoluminescence and Thermal Stability of $BaMgAl_{10}O_{17}$: $Eu^{2+}$ under VUV and UV Excitation, *Opt. Mater.*, 2008, **30**, 930–934.

21 Y. Liu, F. Li, Q. L. Liu and Z. G. Xia, Synergetic Effect of Postsysthetic Water Treatment on the Enhanced Photoluminescence and Stability of $CsPbX_3$ ($X = Cl$, Br, I) Perovskite Nanocrystals, *Chem. Mater.*, 2018, **30**, 6922–6929.

22 J. Pichaandi, K. A. Abel, N. J. J. Johnson and F. C. van Veggel, Long-Term Colloidal Stability and Photoluminescence Retention of Lead-Based Quantum Dots in Saline Buffers and Biological Media through Surface Modification, *Chem. Mater.*, 2013, **25**, 2035–2044.

23 D. Y. Pan, J. C. Zhang, Z. Li, C. Wu, X. M. Yan and M. H. Wu, Observation of PH-, Solvent-, Spin-, and Excitation-Dependent Blue Photoluminescence from Carbon Nanoparticles, *Chem. Commun.*, 2010, **46**, 3681–3683.

24 Y. Wei, Z. Y. Cheng and J. Lin, An overview on enhancing the stability of lead halide perovskite quantum dots and their applications in phosphor-converted LEDs, *Chem. Soc. Rev.*, 2019, **48**, 310–350.

25 B. J. Bohn, Y. Tong, M. Gramlich, M. L. Lai, M. Doḃlinger, K. Wang, R. L. Z. Hoye, P. Mul·ĺl·ler-Buschbaum, S. D. Stranks, A. S. Urban, L. Polavarapu and J. Feldmann, Boosting tunable blue luminescence of halide perovskite nanoplatelets through postsynthetic surface trap repair, *Nano Lett.*, 2018, **18**, 5231–5238.

26 P. C. Tsai, J. Y. Chen, E. Ercan, C. C. Chueh, S. H. Tung and W. C. Chen, Uniform luminous perovskite nanofibers with color-tunability and improved stability prepared by one-step core/shell electrospinning, *Small*, 2018, **14**, 1704379.

27 H. C. Wang, S. Y. Lin, A. C. Tang, B. P. Singh, H. C. Tong, C. Y. Chen, Y. C. Lee, T. L. Tsai and R. S. Liu, Mesoporous Silica Particles Integrated with All-Inorganic $CsPbBr_3$ Perovskite Quantum-Dot Nanocomposites (MP-PQDs) with High Stability and Wide Color Gamut Used for Backlight Display, *Angew. Chem., Int. Ed.*, 2016, **55**, 7924–7929.

28 M. Zhao, Z. G. Xia, X. X. Huang, L. X. Ning, R. Gautier, M. S. Molokeev, Y. Y. Zhou, Y. C. Chuang, Q. Y. Zhang, Q. L. Liu and K. R. Poeppelmeier, Li substituent tuning of LED phosphors with enhanced efficiency, tunable photoluminescence, and improved thermal stability, *Sci. Adv.*, 2019, **5**, 1–7.

29 Z. J. Guan, J. L. Zeng, Z. A. Nan, X. K. Wan, Y. M. Lin and Q. M. Wang, Thiacalix[4]arene: New protection for metal nanoclusters, *Sci. Adv.*, 2016, **2**, e1600323.

30 A. Bilyk, A. K. Hall, J. M. Harrowfield, M. W. Hosseini, B. W. Skelton and A. H. White, Systematic Structural Coordination Chemistry of *p-tert*-Butyltetrathiacalix[4]arene: 1. Group 1 Elements and Congeners, *Inorg. Chem.*, 2001, **40**, 672–686.

31 K. Z. Su, F. L. Jiang, J. J. Qian, J. Pan, J. D. Pang, X. Y. Wan, F. L. Hu and M. C. Hong, Self-assembly of two high-nuclearity manganese calixarene-phosphonate clusters: diamond-like $Mn_{16}$ and drum-like $Mn_{14}$, *RSC Adv.*, 2015, **5**, 33579–33585.

32 Y. Bi, X.-T. Wang, W. Liao, X. Wang, X. Wang, H. Zhang and S. Gao, A $\{Co_{32}\}$ Nanosphere Supported by *p-tert-*

Butylthiacalix[4]arene, *J. Am. Chem. Soc.*, 2009, **131**, 11650–11651.

33 S. T. Wang, X. H. Gao, X. X. Hang, X. F. Zhu, H. T. Han, X. K. Li, W. P. Liao and W. Chen, Calixarene-Based $\{Ni_{18}\}$ Coordination Wheel: Highly Efficient Electrocatalyst for the Glucose Oxidation and Template for the Homogenous Cluster Fabrication, *J. Am. Chem. Soc.*, 2018, **140**, 6271–6277.

34 A. Gehin, S. Ferlay, J. M. Harrowfield, D. Fenske, N. Kyritsakas and M. W. Hosseini, Giant Core–Shell Nanospherical Clusters Composed of 32 Co or 32 Ni Atoms Held by 6 *p-tert*-Butylthiacalix[4]arene Units, *Inorg. Chem.*, 2012, **51**, 5481–5486.

35 X. X. Hang, B. Liu, X. F. Zhu, S. T. Wang, H. T. Han, W. P. Liao, Y. L. Liu and C. H. Hu, Discrete $\{Ni_{40}\}$ Coordination Cage: A Calixarene-Based Johnson-Type ($J_{17}$) Hexadecahedron, *J. Am. Chem. Soc.*, 2016, **138**, 2969–2972.

36 Z. Wang, H. F. Su, Y. W. Gong, Q. P. Qu, Y. F. Bi, C. H. Tung, D. Sun and L. S. Zheng, A hierarchically assembled 88-nuclei silver-thiacalix[4]arene nanocluster, *Nat. Commun.*, 2020, **11**, 308.

37 Y. F. Bi, X. T. Wang, W. P. Liao, X. W. Wang, R. P. Deng, H. J. Zhang and S. Gao, Thiacalix[4]arene-Supported Planar $Ln_4$ ($Ln = Tb^{III}$, $Dy^{III}$) Clusters: Toward Luminescent and Magnetic Bifunctional Materials, *Inorg. Chem.*, 2009, **48**, 11743–11747.

38 J. Y. Ge, J. Ru, F. Gao, Y. Song, X. H. Zhou and J. L. Zuo, Pentanuclear lanthanide pyramids based on thiacalix[4]arene ligand exhibiting slow magnetic relaxation, *Dalton Trans.*, 2015, **44**, 15481–15490.

39 N. Iki, M. Ohta, T. Tanaka, T. Horiuchi and H. Hoshino, A supramolecular sensing system for AgI at nanomolar levels by the formation of a luminescent $Ag^{I}$–$Tb^{III}$–thiacalix[4]arene ternary complex, *New J. Chem.*, 2009, **33**, 23–25.

40 G. Sheldrick, A short history of SHELX, *Acta Crystallogr., Sect. A: Found. Crystallogr.*, 2008, **64**, 112–122.

41 O. Dolomanov, A. Blake, N. Champness, M. Schroder and M. Schroder, OLEX: new software for visualization and analysis of extended crystal structures, *J. Appl. Crystallogr.*, 2003, **36**, 1283–1284.

42 A. L. Spek, Single-crystal structure validation with the program PLATON, *J. Appl. Crystallogr.*, 2003, **36**, 7–11.

43 A. L. Spek, Structure validation in chemical crystallography, *Acta Crystallogr., Sect. D: Biol. Crystallogr.*, 2009, **65**, 148–155.

44 A. L. Spek, What makes a crystal structure report valid, *Inorg. Chim. Acta*, 2018, **470**, 232–237.

45 A. L. Spek, checkCIF validation ALERTS: what they mean and how to respond, *Acta Crystallogr., Sect. E: Crystallogr. Commun.*, 2020, **76**, 1–11.

46 J. D. L. Dutra, T. D. Bispo and R. O. Freire, LUMPAC Lanthanide Luminescence Software: Efficient and User Friendly, *J. Comput. Chem.*, 2014, **35**, 772–775.

47 R. Pearson, Hard and soft acids and bases, *J. Am. Chem. Soc.*, 1963, **85**, 3533–3539.

48 S. Petit, F. Baril-Robert, G. Pilet, C. Reber and D. Luneau, Luminescence spectroscopy of europium(III) and terbium(III) penta-, octa- and nonanuclear clusters with β-diketonate ligands, *Dalton Trans.*, 2009, **34**, 6809–6815.

49 D. I. Alexandropoulos, S. Mukherjee, C. Papatriantafyllopoulou, C. P. Raptopoulou, V. Psycharis, V. Bekiari, G. Christou and T. C. Stamatatos, A New Family of Nonanuclear Lanthanide Clusters Displaying Magnetic and Optical Properties, *Inorg. Chem.*, 2011, **50**, 11276–11278.

50 H. P. Ji, Z. H. Huang, Z. G. Xia, M. S. Molokeev, V. V. Atuchin and S. F. Huang, Cation Substitution Dependent Bimodal Photoluminescence in Whitlockite Structural $Ca^{3-X}Srx(PO_4)_2:Eu^{2+}$ ($0 \leq x \leq 2$) Solid Solution Phosphors, *Inorg. Chem.*, 2014, **53**, 11119–11124.

51 K. Z. Su, F. L. Jiang, J. J. Qian, M. Y. Wu, K. C. Xiong, Y. L. Gai and M. C. Hong, Thiacalix[4]arene-Supported Kite-Like Heterometallic Tetranuclear $Zn^{II}Ln_3^{III}$ ($Ln = Gd$, Tb, Dy, Ho) Complexes, *Inorg. Chem.*, 2013, **52**, 3780–3786.

52 Z. G. Xia, Z. H. Xu, M. Y. Chen and Q. L. Liu, Recent developments in the new inorganic solid-state LED phosphors, *Dalton Trans.*, 2016, **45**, 11214–11232.

53 D. Y. Lin, J. J. Niu, X. B. Liu, X. Zhang, J. Zhang, B. Yu and J. L. Qu, Phasor analysis of fluorescence lifetime data and its application, *Acta Phys. Sin.*, 2020, **69**, 168703.

54 Y. Y. Chen, F. L. Liu, Z. W. Zhang, J. Y. Hong, M. S. Molokeev, I. A. Bobrikov, J. X. Shi, J. B. Zhou and M. W. Wu, A novel $Mn^{4+}$-activated fluoride red phosphor $Cs_{30}(Nb_2O_2F_9)_9(OH)_3 \cdot H_2O:Mn^{4+}$ with good waterproof stability for WLEDs, *J. Mater. Chem. C*, 2022, **10**, 7049–7057.

55 X. F. Wang, J. B. Ke, Y. F. Wang, Y. P. Liang, J. L. He, Z. R. Song, S. X. Lian and Z. X. Qiu, One-Step Design of a Water-Resistant Green-to-Red Phosphor for Horticultural Sunlight Conversion, *ACS Agric. Sci. Technol.*, 2021, **1**, 55–63.

56 K. M. Du, L. J. He, S. Y. Song, J. Feng, Y. Li, M. L. Zhang, H. W. Li, C. Y. Li and H. Zhang, *In Situ* Embedding Synthesis of Highly Stable $CsPbBr_3/CsPb_2Br_5$@PbBr(OH) Nano/Microspheres through Water Assisted Strategy, *Adv. Funct. Mater.*, 2021, **31**, 2103275.

57 T. C. Lang, J. Y. Wang, T. Han, M. S. Cai, S. Q. Fang, Y. Zhong, L. L. Peng, S. X. Cao, B. T. Liu, E. Polisadova, V. Korepanov and A. Yakovlev, Enhancing Structural Rigidity *via* a Strategy Involving Protons for Creating Water-Resistant $Mn^{4+}$-Doped Fluoride Phosphors, *Inorg. Chem.*, 2021, **60**, 1832–1838.

58 J. B. Zhou, Y. F. Wang, Y. Y. Chen, Y. Y. Zhou, B. Milićević, L. Zhou, J. Yan, J. X. Shi, R. S. Liu and M. M. Wu, Single-Crystal Red Phosphors and Their Core–Shell Structure for Improved Water-Resistance for Laser Diodes Applications, *Angew. Chem., Int. Ed.*, 2021, **60**, 3940–3945.

59 P. P. Dang, G. G. Li, X. H. Yun, Q. Q. Zhang, D. J. Liu, H. Z. Lian, M. M. Shang and J. Lin, Thermally stable and highly efficient red-emitting $Eu^{3+}$-doped $Cs_3GdGe_3O_9$ phosphors for WLEDs: non-concentration quenching and negative thermal expansion, *Light: Sci. Appl.*, 2021, **10**, 29.

60 L. P. Jiang, X. Jiang, Y. Zhang, C. X. Wang, P. Liu, G. C. Lv and Y. J. Su, Multiobjective Machine Learning-Assisted Discovery of a Novel Cyan−Green Garnet: Ce Phosphors with Excellent Thermal Stability, *ACS Appl. Mater. Interfaces*, 2022, **14**, 15426–15436.

61 Y. Liu, S. He, D. Wu, X. L. Dong and W. P. Zhou, Broadband NIR Garnet Phosphors with Improved Thermal Stability *via* Energy Transfer, *ACS Appl. Electron. Mater.*, 2022, **4**, 643–650.

62 R. Y. Li, Y. F. Liu, C. X. Yuan, G. Leniec, L. L. Miao, P. Sun, Z. H. Liu, Z. H. Luo, R. Dong and J. Jiang, *Adv. Opt. Mater.*, 2021, **9**, 2100388.

63 T. N. M. Le, C. C. Chiu and J. L. Kuo, A decomposition mechanism for $Mn_2$(DSBDC) metal–organic frameworks in the presence of water molecules, *Phys. Chem. Chem. Phys.*, 2021, **23**, 22794–22803.

64 D. M. Driscoll, R. C. Shiery, M. Balasubramanian, J. L. Fulton and D. C. Cantu, Ionic Contraction across the Lanthanide Series Decreases the Temperature-Induced Disorder of the Water Coordination Sphere, *Inorg. Chem.*, 2021, **61**, 287–294.

65 E. V. Savinkina, I. A. Karavaev, M. S. Grigoriev, G. A. Buzanov and M. N. Davydova, A series of urea complexes with rare-earth nitrates: Synthesis, structure and thermal decomposition, *Inorg. Chim. Acta*, 2022, **532**, 120759.

66 Y. Wang, P. P. Zhang, L. Luo, X. T. Chen, R. Guo and J. Y. Xu, Underlying photoluminescence enhancing mechanism for $Ba_2SiO_4:Eu^{2+}$ phosphor by co-doping $Lu^{3+}$ ion, *J. Lumin.*, 2021, **239**, 118317.

67 H. M. Liu, H. W. Liang, W. Y. Zhang, Q. G. Zeng and D. W. Wen, Improving the thermal stability and luminescent efficiency of $(Ba,Sr)_3SiO_5$: $Eu^{2+}$ phosphors by structure, bandgap engineering and soft chemistry synthesis method, *Chem. Eng. J.*, 2021, **410**, 128367.